



# Deeply self-reconstructing $\text{CoFe}(\text{H}_3\text{O})(\text{PO}_4)_2$ to low-crystalline $\text{Fe}_{0.5}\text{Co}_{0.5}\text{OOH}$ with $\text{Fe}^{3+}\text{--O--Fe}^{3+}$ motifs for oxygen evolution reaction

Shenghua Ye<sup>a,b,1</sup>, Yaqi Lei<sup>a,1</sup>, Tingting Xu<sup>a,1</sup>, Lirong Zheng<sup>c</sup>, Zhida Chen<sup>a</sup>, Xiuyuan Yang<sup>a</sup>, Xiangzhong Ren<sup>a</sup>, Yongliang Li<sup>a</sup>, Qianling Zhang<sup>a,\*</sup>, Jianhong Liu<sup>a,b,\*\*</sup>

<sup>a</sup> Graphene Composite Research Center, College of Chemistry and Environmental Engineering, Shenzhen University, Shenzhen 518060, PR China

<sup>b</sup> Shenzhen Eigen-Equation Graphene Technology Co. Ltd., Shenzhen 518000, PR China

<sup>c</sup> Institute of High Energy Physics Chinese Academy of Sciences, Beijing 100049, PR China

## ARTICLE INFO

### Keywords:

Self-reconstruction

Fe

Phosphate

Oxyhydroxide

Oxygen evolution reaction

## ABSTRACT

In this study, phosphate  $\text{FeCo}(\text{H}_3\text{O})(\text{PO}_4)_2$  nanosheet arrays (NAs) were synthesized using an electrochemical strategy.  $\text{FeCo}(\text{H}_3\text{O})(\text{PO}_4)_2$  NAs as precatalyst could undergo significant self-reconstruction, including leaching of phosphate anions and electro-oxidation of  $\text{Co}^{2+}$  during anodizing at the potential range of oxygen evolution reaction (OER) in 1 M KOH solution, eventually resulting in the formation of  $\text{Fe}_{0.5}\text{Co}_{0.5}\text{OOH}$  NAs with low crystallinity. The high content of Fe in  $\text{Fe}_{0.5}\text{Co}_{0.5}\text{OOH}$  NAs promoted the formation of active  $\text{Fe}^{3+}\text{--O--Fe}^{3+}$  motifs that increased OER occurrence. Additionally, Fe incorporation increased the ratio of the reaction rate constants of oxygen evolution to  $\text{Co}^{3+}/\text{Co}^{4+}$  ( $k_{\text{OER}}/k_{\text{M,ox}}$ ) and enhanced the reaction order on the hydroxyl ion. These factors significantly contributed to the outstanding OER catalytic performances of  $\text{Fe}_{0.5}\text{Co}_{0.5}\text{OOH}$  NAs.

## 1. Introduction

Oxygen evolution reaction (OER) is an important half-cell reaction for water splitting and metal–air batteries [1–4]. However, OER is kinetically sluggish, thus designing applicable catalysts for OER is a crucial process in improving the efficiency of water splitting and metal–air batteries [5]. To date, Ir- and Ru-based catalysts have been considered as the most active OER catalysts, but the scarcity of Ir and Ru and the poor stability that results from the dissolution of Ir and Ru at high anodic overpotential limit their application [6,7]. It is urgent to develop alternative materials composed of low-cost transition metals for OER.

Recently, transition metal-based catalysts such as Ni, Co, and Fe-based sulfides [8–11], phosphides [12–16], nitrides [17], and selenides [18–20] have been intensively explored as efficient OER electrocatalysts. However, recent studies show that these compounds are unstable at the high anodic potential required by the OER process. They should undergo phase conversion to form corresponding metal (oxy) hydroxides that should be part of the real active phase of the OER

process [21–23]. Therefore, the above-mentioned electrocatalysts can be identified as “precatalysts” and the phase conversion that takes place at the anodic potential is called self-reconstruction. These studies show the self-reconstruction chemistry of precatalysts, including the self-reconstruction degrees and reconstruction mechanisms. Additionally, elucidating the property–structure relationship of self-reconstructed metal (oxy)hydroxides is significant for exploring efficient OER electrocatalysts and identifying real OER mechanisms and processes.

Most studies show that self-reconstruction of OER precatalysts only occurs at sub-surface reaction regions at a depth of several nanometers to form the core–shell structure of post-OER catalysts [24–26]. This limited self-reconstruction degree merely generates a small amount of active sites at near-surface regions and leaves a large percentage of inactive atoms in the bulk, which is adverse to the improvement of catalytic activity. In addition, identifying the active layer structure and fundamental reconstruction chemistry of precatalysts is difficult because the thickness of the generated active layer is only several nanometers at near-surface regions. Recently, a small number of precatalysts that

\* Corresponding author.

\*\* Corresponding author at: Graphene Composite Research Center, College of Chemistry and Environmental Engineering, Shenzhen University, Shenzhen 518060, PR China.

E-mail addresses: [zhql@szu.edu.cn](mailto:zhql@szu.edu.cn) (Q. Zhang), [liujh@szu.edu.cn](mailto:liujh@szu.edu.cn) (J. Liu).

<sup>1</sup> Shenghua Ye, Yaqi Lei and Tingting Xu contributed equally to this study.

triggered the deep self-reconstruction needed to completely transform from precatalyst to post-OER catalyst in a new and homogeneous phase. This deep self-reconstruction creates a large percentage of active sites at sub-surface that improve catalytic activity and are convenient for fundamental reconstruction chemistry.

In this study, a potentiostatic oxidation strategy is proposed to synthesize  $\text{Co}_{0.5}\text{Fe}_{0.5}\text{OOH}$  nanosheet arrays (NAs) with a high Fe ratio of approximately 50%. As shown in Scheme 1,  $\text{Co}(\text{OH})_2$  NAs grown on carbon fiber cloth (CFC) by electrodeposition were phosphorized by  $\text{PH}_3$ . Subsequently, dual metal phosphate  $\text{FeCo}(\text{H}_3\text{O})(\text{PO}_4)_2$  NAs were fabricated by potentiostatic oxidation of CoP NAs. Eventually, the  $\text{FeCo}(\text{H}_3\text{O})(\text{PO}_4)_2$  NAs undergo deep self-reconstruction during anodizing at the potential range of OER. This self-reconstruction involves leaching of phosphate anions and electro-oxidation of  $\text{Co}^{2+}$ , eventually resulting in the formation of  $\text{Fe}_{0.5}\text{Co}_{0.5}\text{OOH}$  NAs with low crystallinity and unique  $\text{Fe}^{3+}\text{-O-Fe}^{3+}$  motifs. As prepared,  $\text{Fe}_{0.5}\text{Co}_{0.5}\text{OOH}$  NAs exhibit excellent OER activity.

## 2. Experimental section

### 2.1. Materials

All of the chemical reagents used in this study were purchased from Aladdin (analytical grade).

### 2.2. Catalyst preparation

The synthetic procedures were listed as follows:

- (1)  $\text{Co}(\text{OH})_2$  NAs were grown on CFC by galvanostatic electrodeposition in 10 mL of 0.02 M  $\text{Co}(\text{NO}_3)_2 + 0.1$  M  $\text{NH}_4\text{Cl}$  solution at  $-1.0$  mA  $\text{cm}^{-2}$  for 1 h. The working electrode was CFC (after pretreated in ethanal and concentrated  $\text{HNO}_3$ ), and the counter electrode was a graphite electrode.
- (2) CoP NAs were fabricated by placing  $\text{Co}(\text{OH})_2$  NAs and 0.1 g  $\text{NaH}_2\text{PO}_2$  in two porcelain boats and then heating them at 300 °C using a 5 °C/min ramp rate at this temperature for 120 min under Ar atmosphere.
- (3)  $\text{FeCo}(\text{H}_3\text{O})(\text{PO}_4)_2$  NAs were synthesized by in situ oxidizing CoP NAs in 0.1 M  $(\text{NH}_4)_2\text{Fe}_2(\text{SO}_4)_2$  solution at 1 V vs. SCE for 1000 s, the counter electrode was a graphite electrode.
- (4)  $\text{Fe}_{0.33}\text{Co}_{0.67}\text{OOH}$  NAs were then fabricated by in situ anodic oxidizing  $\text{Co}(\text{OH})_2$  NAs in 0.1 M  $(\text{NH}_4)_2\text{Fe}_2(\text{SO}_4)_2$  solution at 1 V vs. SCE for 1000 s, the counter electrode was a graphite electrode.
- (5)  $\text{CoOOH}$  NAs were fabricated by in situ anodic oxidizing  $\text{Co}(\text{OH})_2$  NAs in solution of 0.1 M  $(\text{NH}_4)_2\text{SO}_4$  at 1 V vs. SCE for 1000 s, the counter electrode was a graphite electrode.

### 2.3. Catalyst characterization

The morphologies of the catalysts were observed by Field emission scan electronic microscopy (JSM-6330 F) and transmission electron microscope (JEM-2010HR). X-ray diffraction (Rigaku D/max 2500/PC)

was employed to investigate the crystallography of materials, and Raman spectroscopy (Renishaw, inVia) were used to characterize the local structure information. FT-IR spectra was recorded by IR Affinity®-1 spectrometer (Shimadzu, Düsseldorf, Germany) using ATR technique. X-ray photoelectron spectroscopy (ESCAKAB 250) was used to analyze the valency-state of elements, C 1 s were calibrated to 284.8 eV. The metal loading and ratio were measured by Inductively coupled plasma-atomic emission spectrometry [TJA IRIS (HR)]. X-ray absorption fine structure were recorded at the 1W1B station of the BSRF.

### 2.4. Electrochemical measurements

A CHI 660E electrochemical analyzer (CH Instruments, Inc., Shanghai, China) was used for electrochemical measurements. A platinum plate was used as a counter electrode, and a mercury oxide electrode was used as a reference electrode. All the potentials were calibrated with respect to the reversible hydrogen electrode (RHE) according to the following equation:  $E(\text{RHE}) = E(\text{vs. HgO/Hg}) + E(\text{HgO/Hg}) + 0.059 \text{ pH}$ . Before measurement, the electrolyte was saturated by  $\text{O}_2$ . The iR correction was applied for all measurements.

### 2.5. Computational details

The OER reaction mechanism of in alkaline were investigated in present work using first-principles calculations as implemented in VASP package. A  $4 \times 4$  supercell of  $\text{CoOOH}$  was used in the whole reaction simulations, which was large enough to eliminate the periodic interactions. The generalized gradient approximation (GGA), using PBE exchange-correlation functional, combining with dispersion interactions through DFT-D<sup>3</sup> methods were carried out in all calculations. The valence electron densities was expanded in a plane wave basis set with a 500 eV cutoff of, and the effect of the core electrons were taken into account by projector-augmented wave (PAW) method. The convergence criteria of  $10^{-6}$  eV was used for the self-consistent energies and the forces for structure relaxation was set as 0.01 eV·Å<sup>-1</sup>. The Brillouin zone was sampled using a Monkhorst-Pack k-points of  $9 \times 9 \times 9$  for  $\text{CoOOH}$  optimization and  $5 \times 5 \times 1$  for OER reaction simulations. The spin polarization was also used in the whole calculations.

The free energies of adsorbed species, were calculated based on the hydrogen electrode (CHE), defining as:

$$\Delta G_{\text{ad}} = \Delta E_{\text{ad}} + \Delta \text{ZPE} - T\Delta S$$

where E, ZPE, and S represented the total energy, zero point energy, and entropy of intermediates, and the thermal-correction energies for each intermediates was set at 298.15 K.

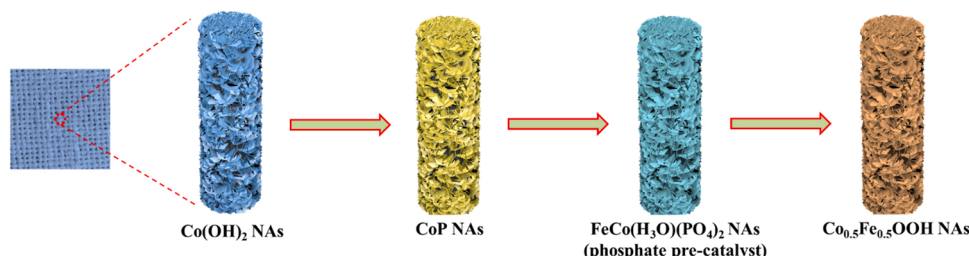
The Gibbs free energy changes of OER were calculated as follows:

$$\Delta G_1 = G(*\text{OH}) + G(\text{H}_2) - G(*) - G(\text{H}_2\text{O})$$

$$\Delta G_2 = G(*\text{O}) + 1/2 G(\text{H}_2) - G(*\text{OH})$$

$$\Delta G_3 = G(*\text{OOH}) + 1/2 G(\text{H}_2) - G(*\text{O}) - G(\text{H}_2\text{O})$$

$$\Delta G_4 = 4.92(\text{eV}) - \Delta G_1 - \Delta G_2 - \Delta G_3$$



Scheme 1. Synthetic process of  $\text{Fe}_{0.5}\text{Co}_{0.5}\text{OOH}$  NAs.

### 3. Results and discussion

#### 3.1. Structural characterization of precatalysts

Scanning electron microscopy (SEM), transmission electron microscope (TEM), and X-ray powder diffraction (XRD) pattern of  $\text{Co}(\text{OH})_2$  NAs are shown in Figs. S1–2 and demonstrate that  $\text{Co}(\text{OH})_2$  nanosheets form a 3D array structure when grown on CFC. CoP NAs were synthesized via annealing with  $\text{NaH}_2\text{PO}_4$  at Ar atmosphere. As shown in Fig. S3, CoP NAs present a similar array structure and polycrystalline nature. The diffraction peak of CoP NAs was indexed to (011), (111), (211), and (020) (JCPDS 29-0497) in XRD pattern (Fig. S4). After potentiostatic oxidation of CoP NAs in 0.1 M  $(\text{NH}_4)_2\text{Fe}(\text{SO}_4)_2$  solution, with an applied potential of 1.0 V vs. SCE, the precatalyst was synthesized (the oxidation was completed within 300 s, as shown in Fig. S5). SEM image of the precatalyst (Fig. 1a) suggested that the 3D array structure was revived, but TEM image (Fig. 1b) suggested that the surface of the nanosheet became loose and porous. High-resolution TEM (HRTEM) image (Fig. 1c) and selected area electron diffraction (SAED) pattern (inserted in Fig. 1c) suggested the low-crystalline nature of the precatalyst that is in accordance with the XRD pattern (Fig. S6). The high-angle annular dark-field scanning transmission electron microscopic (HAADF-STEM) image and corresponding elemental mapping (Fig. 1d) demonstrated that Co, Fe, O, and P were uniformly dispersed throughout the nanosheet, suggesting that Fe and O were introduced during the potentiostatic oxidation process.

To further clarify the chemical structure of the precatalyst, X-ray absorption fine structure (XAFS) spectrum (1W1B station of the Beijing Synchrotron Radiation Facility (BSRF)) was employed. The X-ray absorption near-edge structure (XANES) spectra of the K-edge of Co and Fe are displayed in Fig. 1e and f, respectively. The K-edge position is sensitive to valency. For Co, the K-edge position in the precatalyst is close to that of  $\text{CoO}$  but much lower than that of  $\text{CoOOH}$ , indicating that the valence of Co in the precatalyst is +2. For Fe, the K-edge position is close to that of  $\text{Fe}_2\text{O}_3$ , suggesting that the valence of Fe in the precatalyst is +3. X-ray photoelectron spectroscopy (XPS) was employed to investigate the chemical state of P. From the precatalyst survey, C, O, Co, Fe, and P were identified (Fig. S7). From the P 2p spectrum in Fig. 1g, the

binding energy of P 2p is 134.2 eV, suggesting that P has been oxidized to a valence of +5 during potentiostatic oxidation. Attenuated total reflectance-FTIR (ATR-FTIR) spectrum (Fig. 1h) suggested that an absorption band at  $1065\text{ cm}^{-1}$  was assigned to the symmetrical stretching vibration  $\text{PO}_4^{3-}$  [27–29]. These results demonstrate that the precatalyst should be phosphate constructed by  $\text{Co}^{2+}$ ,  $\text{Fe}^{3+}$ , and  $\text{PO}_4^{3-}$ . The absorption bands at 3000–3500 and  $1630\text{ cm}^{-1}$  belong to the stretching vibration and blending of O–H in  $\text{H}_2\text{O}$  or  $\text{H}_3\text{O}^+$  during hydration. The inductively coupled plasma-atomic emission spectrometry (ICP-AES) measurements suggested that the molar ratio of  $\text{Co}^{2+}$ :  $\text{Fe}^{3+}$ :  $\text{PO}_4^{3-}$  in the precatalyst stage is  $\sim 1:1:2$  (Table S1). However, the above cations and anions ratio results in a unit of exceed negative charge, which cannot meet the charge conservation principle. According to ATR-FTIR spectrum,  $\text{H}_3\text{O}^+$  ion must exist to compensate a unit of exceed negative charge to keep the charge balance, thus the molar ratio of  $\text{Co}^{2+}$ :  $\text{Fe}^{3+}$ :  $\text{H}_3\text{O}^+$ :  $\text{PO}_4^{3-}$  in the precatalyst stage should be inferred as  $1:1:1:2$ . Therefore, the precatalyst should be expressed as  $\text{FeCo}(\text{H}_3\text{O})(\text{PO}_4)_2$  NAs.

#### 3.2. Self-reconstruction study

Subsequently,  $\text{FeCo}(\text{H}_3\text{O})(\text{PO}_4)_2$  NAs underwent consecutive linear sweep voltammetry (LSV) polarizations in 1 M KOH solution. As depicted in Fig. 2a, the first LSV scan exhibited a large redox peak before the OER current, but this redox peak disappeared at the second scan. This phenomenon implied that an irreversible self-reconstruction of the  $\text{FeCo}(\text{H}_3\text{O})(\text{PO}_4)_2$  NAs occurred at the first LSV scan before the onset potential of OER, where a new stable phase (which should be the real catalytic active species) was created by the self-reconstruction (the sample after self-reconstruction is denoted as the post-OER catalyst). After self-reconstruction, the LSV curves of post-OER catalyst remained stable, exhibiting similar appearances in LSV polarizations for OER (Fig. 2b) at subsequent 2000 cycles. Moreover, the post-OER catalyst also exhibited long-term durability without attenuation of catalytic activity (Fig. 2c). The morphology of the post-OER catalyst was investigated. As shown in Fig. 2d, the 3D nanosheet arrays were revived after self-reconstruction, and the nanosheet remained low crystalline (Fig. 2e, f), which is in accordance with the XRD pattern in Fig. S8. The HAADF-STEM image and the corresponding EDS mapping shown in Fig. 2g demonstrated that Co, Fe, and O were uniformly dispersed in the nanosheet, but P was nearly leached out after self-reconstruction.

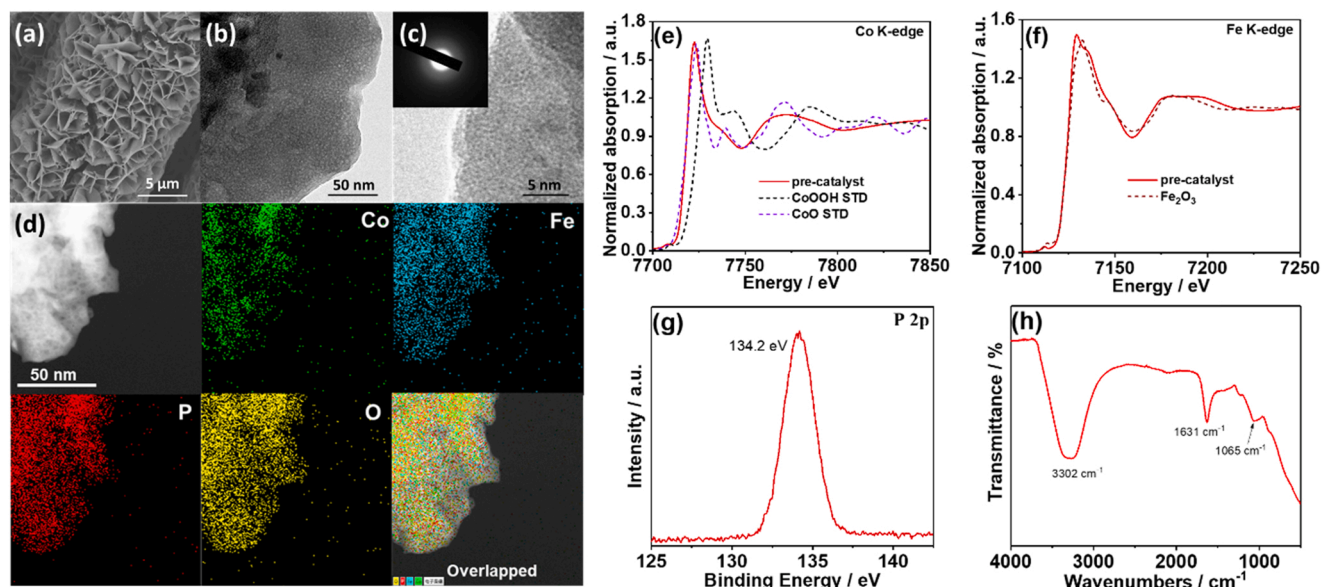


**Fig. 1.** (a) SEM, (b) TEM, and (c) HRTEM images (insert: SAED pattern) of the precatalyst; (d) HAADF-STEM image of the precatalyst and corresponding elemental mapping of Co, Fe, O, and P; XANES of (e) Co K-edge and (f) Fe K-edge of the precatalyst; (g) XPS of the P 2p spectrum of the precatalyst; and (h) ATR-FTIR spectrum of the precatalyst.



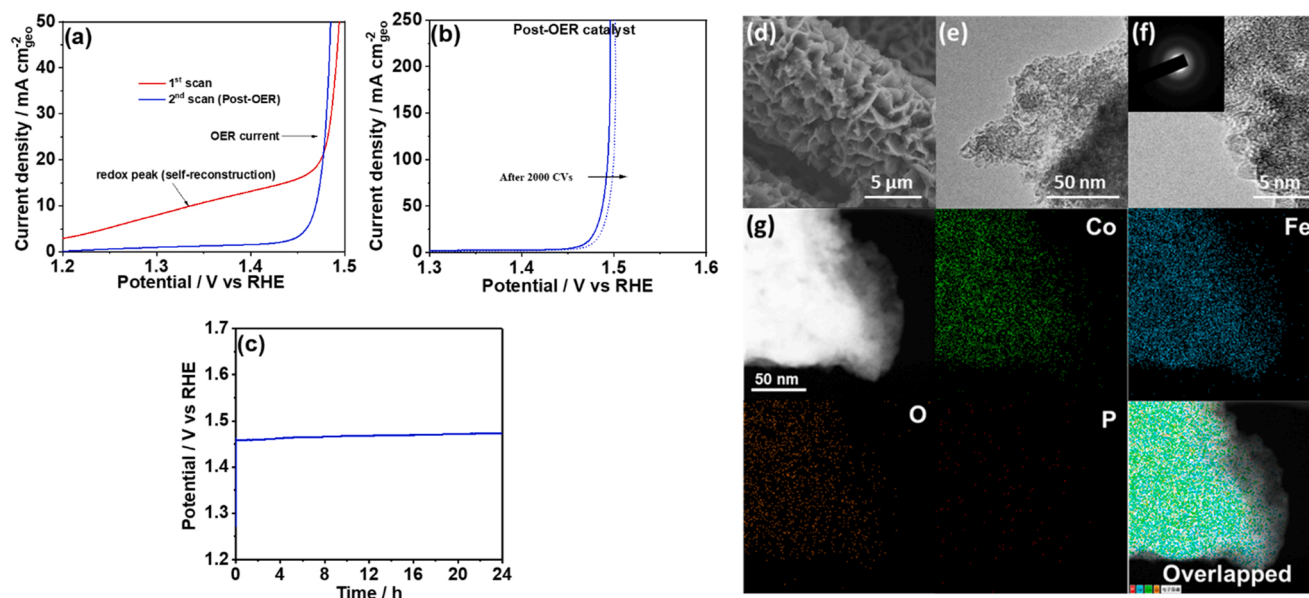


**Fig. 2.** (a) Consecutive LSV polarization curves of  $\text{FeCo}(\text{H}_3\text{O})(\text{PO}_4)_2$  NAs, (b) LSV curves of the post-OER catalyst before and after 2000 CVs, and (c) E-t curve of the post-OER catalyst at a current density of  $10 \text{ mA cm}^{-2}$ . All the above LSV and E-t curves were performed in 1 M KOH solution, the scan rate of LSV was  $5 \text{ mV/s}$ . (d) SEM, (e) TEM, and (f) HRTEM images (insert: SAED pattern) of the post-OER catalyst and (g) HAADF-STEM image of the post-OER catalyst and corresponding elemental mapping of Co, Fe, O, and P.

The components of the post-OER catalyst were determined by ICP-MS. As depicted in Fig. 3a and Table S1, phosphate anions have been almost completely leached out after self-reconstruction (accompanied by minimal stripping of Co and Fe), and the molar ratio of Co/Fe is close to 1. XPS (Fig. S9) and ATR-FTIR spectra (Fig. S10) also suggest that the leaching of phosphate anions occurred during self-reconstruction.  $\text{Co}^{2+}$  has been oxidized to  $\text{Co}^{3+}$  in the post-OER catalyst (Fig. S9c). It can be inferred that  $\text{FeCo}(\text{H}_3\text{O})(\text{PO}_4)_2$  has been reconstructed to oxyhydroxide (MOOH) after OER. According to the ICP-MS result, the post-OER catalyst can be expressed as  $\text{Fe}_{0.5}\text{Co}_{0.5}\text{OOH}$  NAs as follows. To further verify the structure and properties of  $\text{Fe}_{0.5}\text{Co}_{0.5}\text{OOH}$  NAs,  $\text{Fe}_{0.33}\text{Co}_{0.67}\text{OOH}$  NAs and  $\text{CoOOH}$  NAs with similar morphology and loading (Figs. S11–14 and Table S1) were synthesized as counterparts by the same strategy.

As depicted in Fig. 3b, the Raman spectra of  $\text{CoOOH}$  NAs exhibited typical  $\text{A}_1\text{g}$  and  $\text{E}_\text{g}$  vibrational modes of M–O in  $\text{CoOOH}$  [30–32], and  $\text{Fe}_{0.33}\text{Co}_{0.67}\text{OOH}$  NAs also exhibited similar spectra without any characteristics of  $\alpha$ -,  $\beta$ -,  $\gamma$ - $\text{FeOOH}$  and  $\text{FeO}_x$  [33], indicating that Fe has been incorporated into the  $\text{CoOOH}$  matrix.  $\text{Fe}_{0.5}\text{Co}_{0.5}\text{OOH}$  NAs also exhibited the spectral characteristics of  $\text{CoOOH}$ , indicating that  $\text{FeCo}(\text{H}_3\text{O})(\text{PO}_4)_2$  has been reconstructed to MOOH. However, a characteristic dioxygen-bridged  $[\text{di-}\mu\text{-O}(\text{H})] \text{Fe}^{3+}\text{-O-Fe}^{3+}$  motif vibration at approximately  $533 \text{ cm}^{-1}$  could be observed for  $\text{Fe}_{0.5}\text{Co}_{0.5}\text{OOH}$  NAs [34–36], indicating the abnormally high Fe content in  $\text{CoOOH}$  matrix, which generated abundant  $\text{Fe}^{3+}\text{-O-Fe}^{3+}$  motifs in  $\text{Fe}_{0.5}\text{Co}_{0.5}\text{OOH}$  NAs.

To further characterize the chemical state and structure, XAFS was employed. XANES of the Co in Fig. 3c suggested that the K-edge position of the  $\text{Fe}_{0.5}\text{Co}_{0.5}\text{OOH}$  NAs is close to that of  $\text{CoOOH}$  standard (STD) sample, indicating that the valence of Co in the  $\text{Fe}_{0.5}\text{Co}_{0.5}\text{OOH}$  NAs catalyst is +3, rather than that of +2 in precatalyst, which is in accordance with the XPS results. Additionally, the shape of the post-edges (Fig. 3c) and extended X-ray absorption fine structures (EXAFS) (Fig. S15) of  $\text{Fe}_{0.5}\text{Co}_{0.5}\text{OOH}$  NAs,  $\text{Fe}_{0.33}\text{Co}_{0.67}\text{OOH}$  NAs, and  $\text{CoOOH}$  NAs are similar to those of the  $\text{CoOOH}$  STD sample, suggesting that  $\text{Fe}_{0.5}\text{Co}_{0.5}\text{OOH}$  NAs and  $\text{Fe}_{0.33}\text{Co}_{0.67}\text{OOH}$  NAs present a Fe-doped  $\text{CoOOH}$  structure. In addition, Fourier transformed EXAFS (FT-EXAFS) is a powerful method for characterizing coordinative geometry. As shown in Fig. 3d,  $\text{Fe}_{0.5}\text{Co}_{0.5}\text{OOH}$  NAs and  $\text{Fe}_{0.33}\text{Co}_{0.67}\text{OOH}$  NAs present similar coordinative geometry of  $\text{CoOOH}$  with Co–O and Co–M (M = Co,

Fe) (dioxygen-bridged  $[\text{di-}\mu\text{-O}(\text{H})]$  octahedrons) pathways. The fitting curves and parameters of EXAFS are shown in Fig. S16 and Table S2. These findings suggest that the lengths of the Co–O and  $[\text{di-}\mu\text{-O}(\text{H})]$  Co–M pathways are 1.91 and 2.85 Å and the coordinative number (CN) of them are lower than those of the  $\text{CoOOH}$  STD, indicating the structural defects in low-crystalline materials. Moreover, a weak peak, assigned to the Co–M pathway of monooxygen-bridged  $[\text{mono-}\mu\text{-O}(\text{H})]$  octahedrons, was seen in  $\text{Fe}_{0.5}\text{Co}_{0.5}\text{OOH}$  NAs but was weaker and absent in  $\text{Fe}_{0.33}\text{Co}_{0.67}\text{OOH}$  NAs and  $\text{CoOOH}$  NAs respectively (Fig. 3d), suggesting that Fe incorporation induced the formation of  $[\text{mono-}\mu\text{-O}(\text{H})]$   $\text{CoO}_6$  octahedrons. In addition, the valency of Fe in  $\text{Fe}_{0.5}\text{Co}_{0.5}\text{OOH}$  NAs and  $\text{Fe}_{0.33}\text{Co}_{0.67}\text{OOH}$  NAs is similar (Fig. 3e), as is the coordinative geometry of the Fe–O and Fe–M pathways present in  $\text{Fe}_{0.5}\text{Co}_{0.5}\text{OOH}$  NAs and  $\text{Fe}_{0.33}\text{Co}_{0.67}\text{OOH}$  NAs (Fig. 3f and S17–18, and Table S3). The CN of Fe–O is 6, suggesting that Fe presents in  $\text{FeO}_6$  octahedrons. Moreover, an obvious split in Fe–M distances at 2.99 and 3.46 Å indicated that a large amount of  $[\text{mono-}\mu\text{-O}(\text{H})] \text{FeO}_6$  octahedrons exist [37]. The  $\text{mono-}\mu\text{-O}(\text{H})$  bridging of  $\text{MO}_6$  could be explained by an aggregation of metal-oxo octahedrons undergoing condensation, where hydrated oxyhydroxide layers attaching end-by-end through  $\text{mono-}\mu\text{-O}(\text{H})$  bridging to generate steps [37,38]. From EXAFS results we can deduce that Fe incorporation induced the condensation through  $[\text{mono-}\mu\text{-O}(\text{H})] \text{MO}_6$  octahedrons to generate steps in the oxyhydroxides. Therefore, the structure of  $\text{Fe}_{0.33}\text{Co}_{0.67}\text{OOH}$  NAs can be inferred as demonstrated in Fig. 3g(ii). Considering the  $[\text{di-}\mu\text{-O}(\text{H})] \text{Fe}^{3+}\text{-O-Fe}^{3+}$  motifs in  $\text{Fe}_{0.5}\text{Co}_{0.5}\text{OOH}$  NAs, the structure of  $\text{Fe}_{0.5}\text{Co}_{0.5}\text{OOH}$  NAs can be described as demonstrated in Fig. 3g(iii).

With a molar ratio of Co/Fe  $\sim 1$ , particularly during OER, phosphate  $\text{FeCo}(\text{H}_3\text{O})(\text{PO}_4)_2$  deeply self-constructed to MOOH. Previous research revealed that the ratio of Fe/Co in  $\text{Fe}_x\text{Co}_{1-x}\text{OOH}$  should be lower than  $1/2$  ( $0 \leq x \leq 0.33$ ) [39] because the  $\text{Fe}^{3+}\text{-O-Fe}^{3+}$  motif is prevented from forming because of the strong static repulsion [34]. However, the high content of Fe in  $\text{Fe}_{0.5}\text{Co}_{0.5}\text{OOH}$  NAs implies that this limitation was overcome.

### 3.3. Electrochemical study

The OER performances were studied in 1.0 M KOH solution. The polarization curves after iR correction are shown in Fig. 4a. The pristine

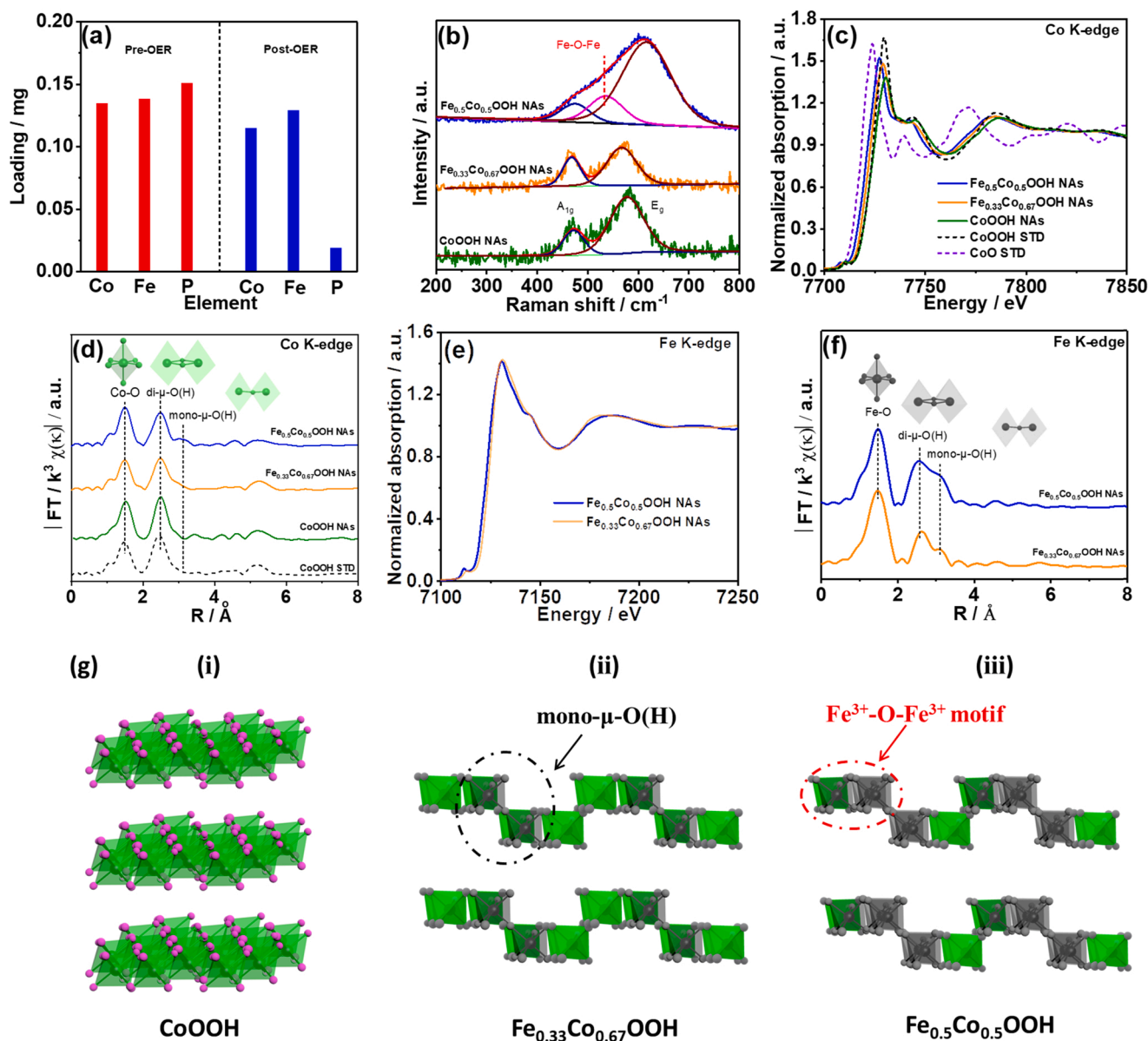


**Fig. 3.** (a) Loading variation of Co, Fe, and P in the catalyst before and after the OER process; (b) Raman spectra of the  $\text{Fe}_{0.5}\text{Co}_{0.5}\text{OOH}$  NAs,  $\text{Fe}_{0.33}\text{Co}_{0.67}\text{OOH}$  NAs, and  $\text{CoOOH}$  NAs; (c, e) XANES and (d, f) FT-EXAFS of the Co K-edge and Fe K-edge, respectively; (g) structural schemes of (i)  $\text{CoOOH}$ , (ii)  $\text{Fe}_{0.33}\text{Co}_{0.67}\text{OOH}$ , and (iii)  $\text{Fe}_{0.5}\text{Co}_{0.5}\text{OOH}$ .

CFC and  $\text{FeOOH}$  (Figs. S19–20) displayed a negligible activity. To reach a current density of  $10 \text{ mA cm}^{-2}$ ,  $\text{Fe}_{0.5}\text{Co}_{0.5}\text{OOH}$  NAs exhibited the lowest overpotential ( $1.457 \text{ V}$ ,  $\eta_{10} = 227 \text{ mV}$ ) compared to  $\text{Fe}_{0.33}\text{Co}_{0.67}\text{OOH}$  NAs ( $1.499 \text{ V}$ ,  $\eta_{10} = 269 \text{ mV}$ ) and  $\text{CoOOH}$  NAs ( $1.564 \text{ V}$ ,  $\eta_{10} = 334 \text{ mV}$ ). They were even superior to  $\text{IrO}_2$  ( $1.521 \text{ V}$ ,  $\eta_{10} = 291 \text{ mV}$ ; Fig. S21), indicating that  $\text{Fe}_{0.5}\text{Co}_{0.5}\text{OOH}$  NAs have excellent OER activity. The small redox peak at  $1.25\text{--}1.40 \text{ V}$  can be assigned to the  $\text{Co}^{3+}/\text{Co}^{4+}$  transition [40]. This redox peak might affect the exact value of  $\eta_{10}$ . Thereupon, the LSV curves were performed from high to low potential to avoid this interference [41,42]. As shown in Fig. 4b, the value of  $\eta_{10}$  in the inverted curve is  $220 \text{ mV}$ , thus the redox peak of  $\text{Co}^{3+}/\text{Co}^{4+}$  did not obviously affect the value of  $\eta_{10}$ . A similar phenomenon was observed for  $\text{Fe}_{0.5}\text{Co}_{0.5}\text{OOH}$  NAs and  $\text{CoOOH}$  NAs (Fig. S22). The Tafel slope (Fig. 4c) of  $\text{Fe}_{0.5}\text{Co}_{0.5}\text{OOH}$  NAs ( $32.74 \text{ mV dec}^{-1}$ ) was much lower than that of  $\text{CoOOH}$  NAs ( $52.31 \text{ mV dec}^{-1}$ ) and close to that of  $\text{Fe}_{0.33}\text{Co}_{0.67}\text{OOH}$  NAs ( $33.75 \text{ mV dec}^{-1}$ ), suggesting that  $\text{Fe}_{0.5}\text{Co}_{0.5}\text{OOH}$  NAs have rapid kinetics and share similar reactive mechanisms with  $\text{Fe}_{0.33}\text{Co}_{0.67}\text{OOH}$  NAs. The catalytic activity of

$\text{Fe}_{0.5}\text{Co}_{0.5}\text{OOH}$  NAs is also superior to most state-of-the-art Co-based catalysts (Table S4) and Fe doped Ni, Co-based LDHs (Table S5). The surface area of the active geometrically specified electrode is not representative of the material's surface area for true catalytic activity [43] because surface topography and loading are not taken into account. In order to further verify the activities of  $\text{Fe}_{0.5}\text{Co}_{0.5}\text{OOH}$  NAs,  $\text{Fe}_{0.33}\text{Co}_{0.67}\text{OOH}$  NAs, and  $\text{CoOOH}$  NAs, the electrochemically active area (ECSA) was obtained by testing the electrochemical double-layer capacitance ( $C_{dl}$ ) derived from cyclic voltammetric (CV) curves (Fig. S23). After the normalization of the LSV curves to the ECSA,  $\text{Fe}_{0.5}\text{Co}_{0.5}\text{OOH}$  NAs still displayed much higher catalytic activity, as depicted in Fig. 4d, indicating intrinsic activity improvement of  $\text{Fe}_{0.5}\text{Co}_{0.5}\text{OOH}$  NAs.

In addition, when the catalytic current density is normalized to the mass of catalysts,  $\text{Fe}_{0.5}\text{Co}_{0.5}\text{OOH}$  NAs still exhibit the highest catalytic activity (Fig. S24). The results of the electrochemical impedance spectroscopy (EIS) are shown in Fig. 4e, after which the corresponding circuit model fitting analysis was performed (Fig. S25 and Table S6). The

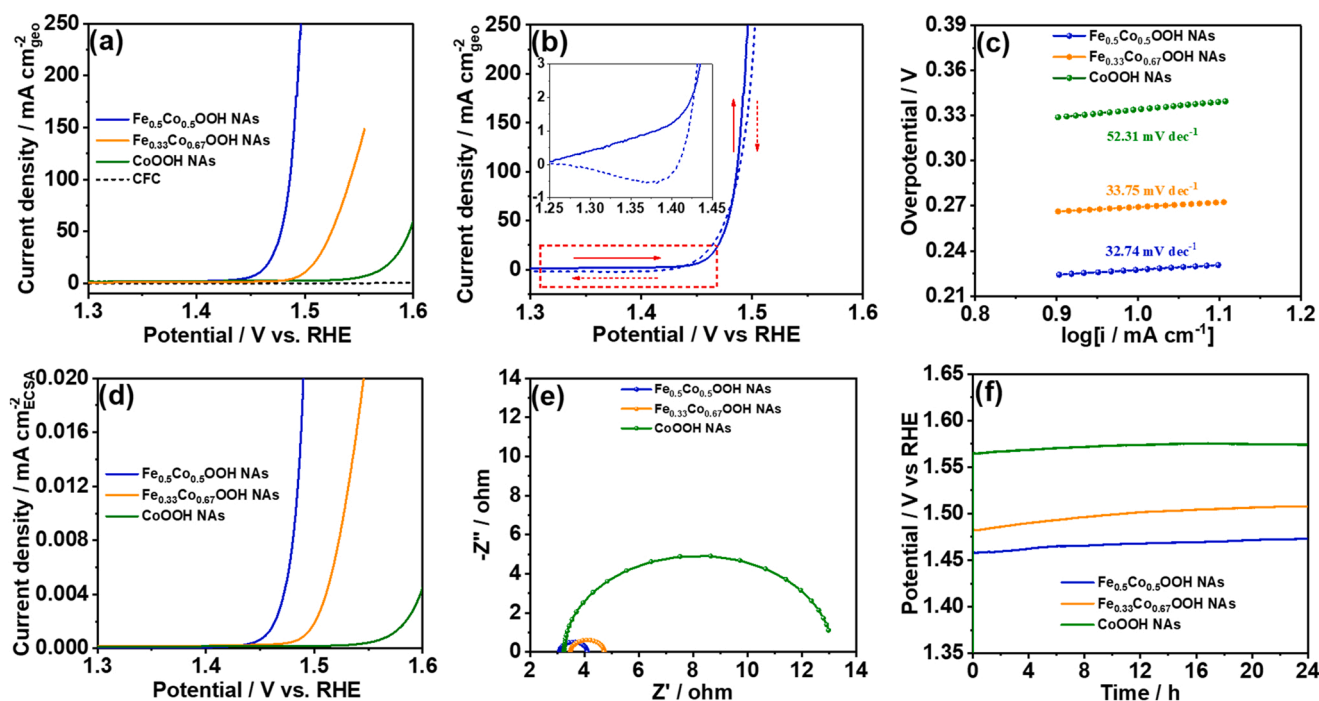


**Fig. 4.** (a) LSV curves of  $\text{Fe}_{0.5}\text{Co}_{0.5}\text{OOH}$  NAs,  $\text{Fe}_{0.33}\text{Co}_{0.67}\text{OOH}$  NAs, and  $\text{CoOOH}$  NAs in 1 M KOH at a scan rate of 5 mV/s; (b) LSV curves of  $\text{Fe}_{0.5}\text{Co}_{0.5}\text{OOH}$  NAs swept from low to high potential and high to low potential; (c) Tafel plots of  $\text{Fe}_{0.5}\text{Co}_{0.5}\text{OOH}$  NAs,  $\text{Fe}_{0.33}\text{Co}_{0.67}\text{OOH}$  NAs, and  $\text{CoOOH}$  NAs with a current density normalized to the ECSA; (d) LSV curves of  $\text{Fe}_{0.5}\text{Co}_{0.5}\text{OOH}$  NAs,  $\text{Fe}_{0.33}\text{Co}_{0.67}\text{OOH}$  NAs, and  $\text{CoOOH}$  NAs at a current density of  $10 \text{ mA cm}^{-2}$ ; (e) EIS plots at 1.549 V; and (f) E-t curves of  $\text{Fe}_{0.5}\text{Co}_{0.5}\text{OOH}$  NAs,  $\text{Fe}_{0.33}\text{Co}_{0.67}\text{OOH}$  NAs, and  $\text{CoOOH}$  NAs at a current density of  $10 \text{ mA cm}^{-2}$ .

equivalent circuit of EIS consisted of solution resistance ( $R_s$ ) and charge transfer resistant ( $R_{CT}$ ). Obviously,  $\text{Fe}_{0.5}\text{Co}_{0.5}\text{OOH}$  NAs displayed the lowest  $R_{CT}$  (0.943  $\Omega$ ), which was lower than that of  $\text{Fe}_{0.33}\text{Co}_{0.67}\text{OOH}$  NAs and  $\text{CoOOH}$  NAs, illustrating a rapid electron transfer.

Durabilities of the as-prepared catalysts were further evaluated by long-term test. As depicted in Fig. 2b, the activity of  $\text{Fe}_{0.5}\text{Co}_{0.5}\text{OOH}$  NAs remained stable after 2000 cycles. By contrast, there was slight attenuation exhibited in the activity of  $\text{Fe}_{0.33}\text{Co}_{0.67}\text{OOH}$  NAs and  $\text{CoOOH}$  NAs (Fig. S26). The galvanostatic test at  $10 \text{ mA cm}^{-2}$  (Fig. 4f) also indicated that  $\text{Fe}_{0.5}\text{Co}_{0.5}\text{OOH}$  NAs remained the best catalytic activity during 24 h electrolysis, and the  $\text{Fe}^{3+}\text{--O--Fe}^{3+}$  motif vibration also could be observed after durability test as shown in Fig. S29c. Consequently,  $\text{Fe}_{0.5}\text{Co}_{0.5}\text{OOH}$  NAs exhibited satisfactory stability.

### 3.4. Oxygen evolution reaction mechanism study

The origination of OER activity and the catalytic mechanisms of  $\text{Fe}_{0.5}\text{Co}_{0.5}\text{OOH}$  NAs were further investigated.

There are two alternative OER pathways: the lattice oxygen oxidation mechanism (LOM) and the conventional adsorbate evolution mechanism (AEM). As shown in Fig. S30, LOM involves coupling of lattice oxygen and adsorbed oxygen to form the O–O bond, thus negative  $\text{O}_2^{2-}$  is characteristic intermediate [44,45]. Tetramethylammonium cation ( $\text{TMA}^+$ ) can attack the  $\text{O}_2^{2-}$  and retard the LOM process, therefore tetramethylammonium hydroxide (TMAOH) was employed as a chemical probe for  $\text{O}_2^{2-}$  species to recognize the occurrence of LOM [46]. The OER was performed in 1 M TMAOH to preliminarily study the reactive pathway [44–46]. As shown in Fig. S31, the activities of  $\text{Fe}_{0.5}\text{Co}_{0.5}\text{OOH}$  NAs,  $\text{Fe}_{0.33}\text{Co}_{0.67}\text{OOH}$  NAs, and  $\text{CoOOH}$  NAs in 1 M TMAOH exhibited obvious attenuation compared with those in 1 M KOH, indicating that they obey LOM, rather than AEM. Additionally, the deuterium kinetic isotope effects (KIEs) can reflect the kinetic information of the proton transfer in water oxidation reactions. The LSV curves of the samples in the 1.0 M NaOD  $\text{D}_2\text{O}$  solution exhibited slightly lower current densities (within 1.5) in comparison with those in the 1.0 M NaOH  $\text{H}_2\text{O}$  solution

(Figs. S32–34). These results suggest that the OER processes of  $\text{Fe}_{0.5}\text{Co}_{0.5}\text{OOH}$  NAs,  $\text{Fe}_{0.33}\text{Co}_{0.67}\text{OOH}$  NAs, and  $\text{CoOOH}$  NAs obey a LOM, but the rate-determining step is not involved with the cleavage of the O–H bond [47,48]. These results are consistent with the previous studies.

In the previous studies, the Fe site has optimal absorption energy for the oxygen-containing intermediates, suggesting that Fe obviously improves the OER activity of layered double hydroxides. Therefore, the abnormally high Fe content in  $\text{Fe}_{0.5}\text{Co}_{0.5}\text{OOH}$  NAs contributed to its improved OER activity. Raman spectra indicated the existence of  $\text{Fe}^{3+}\text{--O--Fe}^{3+}$  motifs in  $\text{Fe}_{0.5}\text{Co}_{0.5}\text{OOH}$  NAs, implying that neighboring  $\text{FeO}_6$  octahedrons were created by edge-sharing (Fig. 3g), which did not occur in conventional structures because of strong static repulsion. According to the previous research, these  $\text{Fe}^{3+}\text{--O--Fe}^{3+}$  couples act as stable high-valent motifs and are responsible for the significantly improved OER intrinsic activity,  $\text{Fe}^{3+}\text{--O--Fe}^{3+}$  motifs are likely to be more active site than isolated  $\text{FeO}_6$  sites [34]. Furthermore, density functional theory (DFT) calculation was used to reveal the exact adsorption behavior of oxygen-contained intermediates on  $\text{Fe}^{3+}\text{--O--Fe}^{3+}$  motifs. As shown in Figs. S35–36,  $^*\text{OH}$  and  $^*\text{O}$  preferentially were adsorbed on  $\text{Fe}^{3+}\text{--O--Fe}^{3+}$  motifs which located at the steps of oxyhydroxide layers. However,  $^*\text{OOH}$  trend to be adsorbed on  $[\text{di-}\mu\text{-O}(\text{OH})]$  Co–Fe sites via formation of O–O bridged linkage, suggesting the synergistic catalysis of Co and Fe sites. Moreover, free energy diagrams shown in Fig. S37 suggests that the energy barrier of OER rate-determining step decreased with increase of  $\text{Fe}^{3+}\text{--O--Fe}^{3+}$  motifs.

In addition to Fe sites, previous studies suggested that in-situ generated high-valent transition metallic sites (such as  $\text{Ni}^{3+}$  or  $\text{Co}^{4+}$ ) also could be considered as active sites for OER [49]. For this reason, the OER cycles could be described via a simplified scheme (Fig. 5a), where the buildup of oxidation equivalents from  $\text{Co}^{3+}$  to  $\text{Co}^{4+}$  triggered the O–O bond formation and subsequently released  $\text{O}_2$ , restoring  $\text{Co}^{4+}$  back to  $\text{Co}^{3+}$ . These two processes were quantified by the reaction rate constants of  $k_{\text{M,ox}}$  and  $k_{\text{OER}}$ , respectively. The accumulation of  $\text{Co}^{4+}$  during OER is related to the ratio of  $k_{\text{OER}}/k_{\text{M,ox}}$ , so it can be employed to reveal



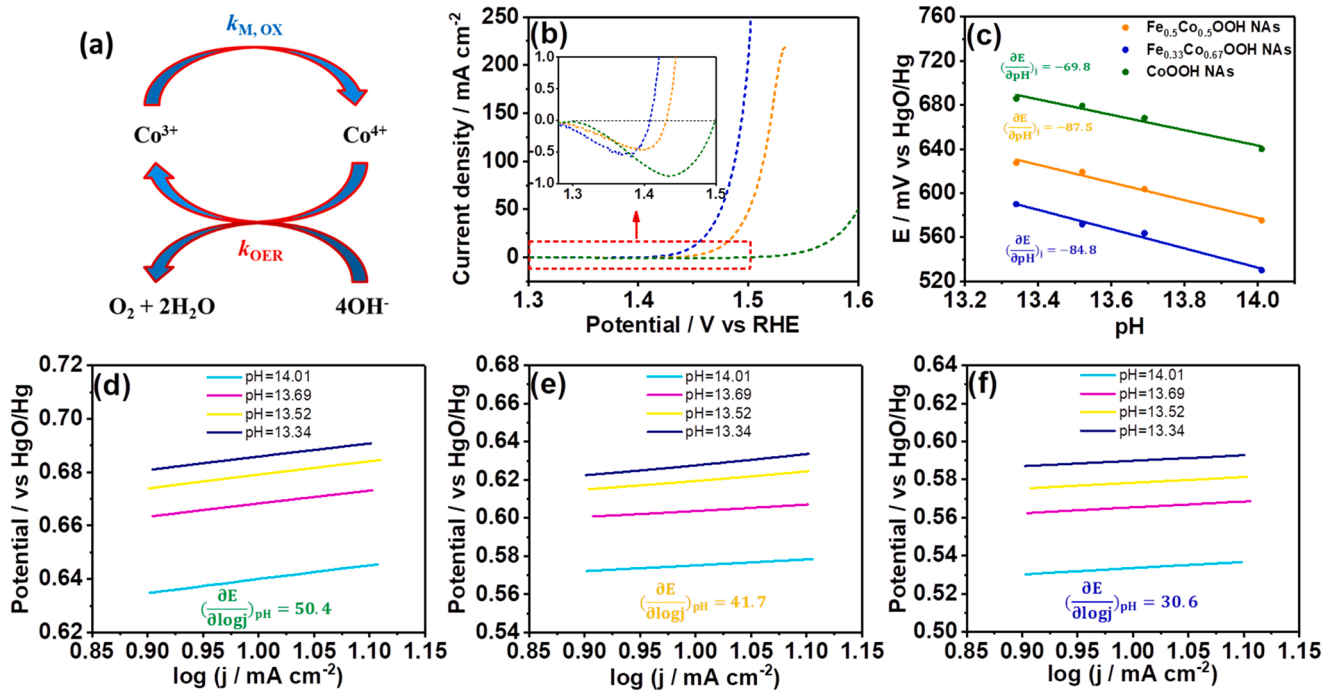


**Fig. 5.** (a) Simplified scheme of the OER cycle with the metal oxidation rate constant,  $k_{M,ox}$ , and the catalytic OER rate constant,  $k_{OER}$ ; (b) LSV curves of  $Fe_{0.5}Co_{0.5}OOH$  NAs,  $Fe_{0.33}Co_{0.67}OOH$  NAs, and  $CoOOH$  NAs swept from high to low potential in 1 M KOH solution at 5 mV/s; (c) fitting plot of the potentials at 10 mA  $cm^{-2}$  vs. the pH value of the electrolytes; and OER activities of (d)  $CoOOH$  NAs, (e)  $Fe_{0.33}Co_{0.67}OOH$  NAs, and (f)  $Fe_{0.5}Co_{0.5}OOH$  NAs in Fe-free KOH solutions with different pH values (14.01, 13.69, 13.52, and 13.34).

the kinetics of OER [37,49]. The accumulation of  $Co^{4+}$  during OER was quantified by the redox peak of  $Co^{3+}/Co^{4+}$ . To avoid the interference of the OER catalytic current, the redox peak was observed by an inverse scan. As depicted in Fig. 5b, the areas of the redox peak in  $Fe_{0.5}Co_{0.5}OOH$  NAs and  $Fe_{0.33}Co_{0.67}OOH$  NAs were smaller than those of  $CoOOH$  NAs, indicating that Fe incorporation dramatically increased  $k_{OER}/k_{M,ox}$ , thus the accumulation of  $Co^{4+}$  was released and the overall OER kinetics were accelerated.

The OER activities of  $Fe_{0.5}Co_{0.5}OOH$  NAs,  $Fe_{0.33}Co_{0.67}OOH$  NAs, and  $CoOOH$  NAs exhibited pH dependence (Fig. S38). The catalytic activity increased as the  $OH^-$  concentration increased. The following equation describes the reaction kinetics:

$$j = k[OH^-]^n = k\left(\frac{10^{-14}}{[H^+]}\right)^n = k'\left(\frac{1}{[H^+]}\right)^n, \quad (1)$$

$$n = \frac{d \log j}{d \log [H^+]}, \quad (2)$$

where  $k$  and  $k'$  are defined as general OER reaction rate constants.

According to the mathematical relationship:

$$d \log j = \left(\frac{\partial \log j}{\partial E}\right)_{pH} dE + \left(\frac{\partial \log j}{\partial pH}\right)_E dpH. \quad (3)$$

The following equation can be inferred:

$$n = \left(\frac{\partial \log j}{\partial pH}\right)_E = -\left(\frac{\partial E}{\partial pH}\right)_j \left(\frac{\partial \log j}{\partial E}\right)_{pH}. \quad (4)$$

Here, the  $\left(\frac{\partial E}{\partial pH}\right)_j$  item was determined by Fig. 5c, and the  $\left(\frac{\partial \log j}{\partial E}\right)_{pH}$  item was determined by the Tafel slope (Tafel slope is  $\left(\frac{\partial \log j}{\partial E}\right)_{pH}^{-1}$ ). These three samples exhibited similar Tafel slopes at a pH range of 13.34–14.01 (Fig. 5d–f: the average values of the Tafel slopes were used for calculation). According to Eq. (4), the catalytic activity has an

approximate one-order dependence on the  $OH^-$  concentration for  $CoOOH$  NAs, which is in accordance with previous studies [50]. However,  $Fe_{0.33}Co_{0.67}OOH$  NAs exhibited approximately two-order dependence, and  $Fe_{0.5}Co_{0.5}OOH$  NAs exhibited three-order dependence on  $OH^-$  concentration. Therefore, Fe incorporation increased the reactive order of the rate-determining step. The unique  $Fe^{3+}-O-Fe^{3+}$  motifs further increased the reactive order, eventually accelerating the OER kinetics.

#### 4. Conclusion

In summary, we present an electrochemical strategy to synthesize the phosphate  $FeCo(H_3O)(PO_4)_2$  NAs grown on CFC as precatalyst for OER. During the OER process, irreversible deep self-reconstruction of  $FeCo(H_3O)(PO_4)_2$  NAs resulted in the formation of  $Fe_{0.5}Co_{0.5}OOH$  NAs. The high content of Fe in  $Fe_{0.5}Co_{0.5}OOH$  NAs broke the limit that the ratio of Fe/Co in  $Fe_xCo_{1-x}OOH$  should be lower than 1/2 and promoted the formation of active  $Fe^{3+}-O-Fe^{3+}$  motifs that are regarded as optimal catalytic sites. Moreover, the mechanism of Fe incorporation was studied in detail, and experimental evidence revealed that Fe incorporation dramatically increased  $k_{OER}/k_{M,ox}$ , thus greatly improving the OER kinetics. Importantly, Fe incorporation increased the pH dependence of OER activity, thus the reactive order on  $OH^-$  concentration was enhanced as Fe content increased.

#### CRediT authorship contribution statement

**Shenghua Ye, Yaqi Lei and Tingting Xu** contributed equally to this study. **Yaqi Lei and Tingting Xu**: Structural characterization and electrochemical measurements. **Shenghua Ye**: Guided the experiments and performed data and theoretical analysis. **Lirong Zheng**: XAFS measurements and EXAFS fitting. **Zhida Chen and Xiuyuan Yang**: Help to the electrochemical measurements. **Xiangzhong Ren and Yongliang Li**: Help to the data analysis and academic writing. **Qianling Zhang**: Convinced the experimental results and discussion. **Jianhong Liu**:

Supervised the writing and reviewing.

## Declaration of Competing Interest

The authors declare that they have no known competing financial interests or personal relationships that could have appeared to influence the work reported in this paper.

## Acknowledgements

We thank the financial support of National Key Research and Development Program Funding (No. 2020YFC1909600), Shenzhen Key Projects of Technological Research (JSGG20200925145800001), Shenzhen Basic Research Project (Nos. JCYJ20190808145203535 and JCYJ20190808144413257), Natural Science Foundation of Guangdong Province (No. 2020A1515010379), and the Major Industrial Projects of Shenzhen (No. s2017001850011). We are grateful to the Instrumental Analysis Center of Shenzhen University (Xili Campus) for providing the facilities for our material analyzes. We are also grateful to Huasuan Technology Co., Ltd. for providing theoretical calculation.

## Appendix A. Supporting information

Supplementary data associated with this article can be found in the online version at [doi:10.1016/j.apcatb.2021.120986](https://doi.org/10.1016/j.apcatb.2021.120986).

## References

- [1] F. Song, L.C. Bai, A. Moysiadou, S. Lee, C. Hu, L. Liardet, X.L. Hu, Transition metal oxides as electrocatalysts for the oxygen evolution reaction in alkaline solutions: an application-inspired renaissance, *J. Am. Chem. Soc.* 140 (2018) 7748–7759.
- [2] N.T. Suen, S.F. Hung, Q. Quan, N. Zhang, Y.J. Xu, H.M. Chen, Electrocatalysis for the oxygen evolution reaction: recent development and future perspectives, *Chem. Soc. Rev.* 46 (2017) 337–365.
- [3] Z.W. Seh, J. Kibsgaard, C.F. Dickens, I. Chorkendorff, J.K. Nørskov, T.F. Jaramillo, Combining theory and experiment in electrocatalysis: insights into materials design, *Science* 355 (2017) eaad4998.
- [4] S. Ye, W. Xiong, P. Liao, L. Zheng, X. Ren, C. He, Q. Zhang, J. Liu, Removing the barrier to water dissociation on single-atom Pt sites decorated with a CoP mesoporous nanosheet array to achieve improved hydrogen evolution, *J. Mater. Chem. A* 8 (2020) 11246–11254.
- [5] J. Song, C. Wei, Z.-F. Huang, C. Liu, L. Zeng, X. Wang, Z.J. Xu, A review on fundamentals for designing oxygen evolution electrocatalysts, *Chem. Soc. Rev.* 49 (2020) 2196–2214.
- [6] J. Kibsgaard, I. Chorkendorff, Considerations for the scaling-up of water splitting catalysts, *Nat. Energy* 4 (2019) 430–433.
- [7] Q. Wang, X. Huang, Z.L. Zhao, M. Wang, B. Xiang, J. Li, Z. Feng, H. Xu, M. Gu, Ultrahigh-loading of Ir single atoms on NiO matrix to dramatically enhance oxygen evolution reaction, *J. Am. Chem. Soc.* 142 (2020) 7425–7433.
- [8] J. Li, D. Chu, H. Dong, D.R. Baker, R. Jiang, Boosted oxygen evolution reactivity by igniting double exchange interaction in spinel oxides, *J. Am. Chem. Soc.* 142 (2020) 50–54.
- [9] B. Fei, Z. Chen, J. Liu, H. Xu, X. Yan, H. Qing, M. Chen, R. Wu, Ultrathinning nickel sulfide with modulated electron density for efficient water splitting, *Adv. Energy Mater.* 10 (2020), 2001963.
- [10] K. Maslana, K. Wenelska, M. Biegun, E. Mijowska, High catalytic performance of tungsten disulfide rods in oxygen evolution reactions in alkaline solutions, *Appl. Catal. B Environ.* 266 (2020), 118575.
- [11] H. Su, S. Song, S. Li, Y. Gao, L. Ge, W. Song, T. Ma, J. Liu, High-valent bimetal Ni3S2/Co3S4 induced by Cu doping for bifunctional electrocatalytic water splitting, *Appl. Catal. B Environ.* 293 (2021), 120225.
- [12] H. Liu, J. Guan, S. Yang, Y. Yu, R. Shao, Z. Zhang, M. Dou, F. Wang, Q. Xu, Metal-organic-framework-derived Co2P nanoparticle/multi-doped porous carbon as a trifunctional electrocatalyst, *Adv. Mater.* 32 (2020), 2003649.
- [13] G. Yuan, J. Bai, L. Zhang, X. Chen, L. Ren, The effect of P vacancies on the activity of cobalt phosphide nanorods as oxygen evolution electrocatalyst in alkali, *Appl. Catal. B Environ.* 284 (2021), 119693.
- [14] X. Li, J. Zhou, C. Liu, L. Xu, C. Lu, J. Yang, H. Pang, W. Hou, Encapsulation of Janus-structured Ni/Ni2P nanoparticles within hierarchical wrinkled N-doped carbon nanofibers: interface engineering induces high-efficiency water oxidation, *Appl. Catal. B Environ.* 298 (2021), 120578.
- [15] S. Wang, P. Yang, X. Sun, H. Xing, J. Hu, P. Chen, Z. Cui, W. Zhu, Z. Ma, Synthesis of 3D heterostructure Co-doped Fe2P electrocatalyst for overall seawater electrolysis, *Appl. Catal. B Environ.* 297 (2021), 120386.
- [16] H. Roh, H. Jung, H. Choi, J.W. Han, T. Park, S. Kim, K. Yong, Various metal (Fe, Mo, V, Co)-doped Ni2P nanowire arrays as overall water splitting electrocatalysts and their applications in unassisted solar hydrogen production with STH 14%, *Appl. Catal. B Environ.* 297 (2021), 120434.
- [17] H. Liu, J. Lei, S. Yang, F. Qin, L. Cui, Y. Kong, X. Zheng, T. Duan, W. Zhu, R. He, Boosting the oxygen evolution activity over cobalt nitride nanosheets through optimizing the electronic configuration, *Appl. Catal. B Environ.* 286 (2021), 119894.
- [18] S. Niu, W.-J. Jiang, Z. Wei, T. Tang, J. Ma, J.-S. Hu, L.-J. Wan, Se-doping activates FeOOH for cost-effective and efficient electrochemical water oxidation, *J. Am. Chem. Soc.* 141 (2019) 7005–7013.
- [19] Z. Chen, M. Chen, X. Yan, H. Jia, B. Fei, Y. Ha, H. Qing, H. Yang, M. Liu, R. Wu, Vacancy occupation-driven polymorphic transformation in cobalt ditelluride for boosted oxygen evolution reaction, *ACS Nano* 14 (2020) 6968–6979.
- [20] D. Xiao, D.-L. Bao, X. Liang, Y. Wang, J. Shen, C. Cheng, P.K. Chu, Experimental and theoretical investigation of the control and balance of active sites on oxygen plasma-functionalized MoSe2 nanosheets for efficient hydrogen evolution reaction, *Appl. Catal. B Environ.* 288 (2021), 119983.
- [21] Nitrides, and phosphides oxygen evolution catalysts or bifunctional catalysts? *ACS Energy Lett.* 2 (2017) 1937–1938.
- [22] N.C.S. Selvam, L.J. Du, B.Y. Xia, P.J. Yoo, B. You, Reconstructed water oxidation electrocatalysts: the impact of surface dynamics on intrinsic activities, *Adv. Funct. Mater.* 31 (2020), 119983.
- [23] S. Li, Z. Li, R. Ma, C. Gao, L. Liu, L. Hu, J. Zhu, T. Sun, Y. Tang, D. Liu, J. Wang, A glass-ceramic with accelerated surface reconstruction toward the efficient oxygen evolution reaction, *Angew. Chem. Int. Ed.* 60 (2021) 3773–3780.
- [24] P.Z. Chen, K. Xu, Z.W. Fang, Y. Tong, J.C. Wu, X.L. Lu, X. Peng, H. Ding, C.Z. Wu, Y. Xie, Metallic Co4N porous nanowire arrays activated by surface oxidation as electrocatalysts for the oxygen evolution reaction, *Angew. Chem. Int. Ed.* 54 (2015) 14710–14714.
- [25] A. Grimaud, A. Demortiere, M. Saubane, W. Dachraoui, M. Duchamp, M. L. Doublet, J.M. Tarascon, Activation of surface oxygen sites on an iridium-based model catalyst for the oxygen evolution reaction, *Nat. Energy* 2 (2017) 16189.
- [26] X. Liu, J. Meng, K. Ni, R. Guo, F. Xia, J. Xie, X. Li, B. Wen, P. Wu, M. Li, J. Wu, X. Wu, L. Mai, D. Zhao, Complete reconstruction of hydrate pre-catalysts for ultrastable water electrolysis in industrial-concentration alkali media, *Cell Rep. Phys. Sci.* 1 (2020), 100241.
- [27] A.A. Salah, P. Jozwiak, K. Zaghbi, J. Garbacz, F. Gendron, A. Mauger, C. M. Julien, FTIR features of lithium-iron phosphates as electrode materials for rechargeable lithium batteries, *Spectrochim. Acta A* 65 (2006) 1007–1013.
- [28] C. Yang, C. Laberty-Robert, D. Batuk, G. Cibi, A.V. Chadwick, V. Pimenta, W. Yin, L. Zhang, J.-M. Tarascon, A. Grimaud, Phosphate ion functionalization of perovskite surfaces for enhanced oxygen evolution reaction, *J. Phys. Chem. Lett.* 8 (2017) 3466–3472.
- [29] J.D. Kubicki, K.W. Paul, L. Kabalan, Q. Zhu, M.K. Mroczek, M. Aryanpour, A.-M. Pierre-Louis, D.R. Strongin, ATR-FTIR and density functional theory study of the structures, energetics, and vibrational spectra of phosphate adsorbed onto goethite, *Langmuir* 28 (2012) 14573–14587.
- [30] A. Moysiadou, S. Lee, C.S. Hsu, H.M. Chen, X.L. Hu, Mechanism of oxygen evolution catalyzed by cobalt oxyhydroxide: cobalt superoxide species as a key intermediate and dioxygen release as a rate-determining step, *J. Am. Chem. Soc.* 142 (2020) 11901–11914.
- [31] C. Pasquini, L. D'Amario, I. Zaharieva, H. Dau, Operando Raman spectroscopy tracks oxidation-state changes in an amorphous Co oxide material for electrocatalysis of the oxygen evolution reaction, *J. Chem. Phys.* 152 (2020), 194202.
- [32] Z.K. Kou, Y. Yu, X.M. Liu, X.R. Gao, L.R. Zheng, H.Y. Zou, Y.J. Pang, Z.Y. Wang, Z. H. Pan, J.-Q. He, S.J. Pennycook, J. Wang, Potential-dependent phase transition and Mo-enriched surface reconstruction of gamma-CoOOH in a heterostructured Co-Mo2C precatalyst enable water oxidation, *ACS Catal.* 10 (2020) 4411–4419.
- [33] D.L.A. de Faria, S. Venancio Silva, M.T. de Oliveira, Raman microspectroscopy of some iron oxides and oxyhydroxides, *J. Raman Spectrosc.* 28 (1997) 873–879.
- [34] Z. Cai, D.J. Zhou, M.Y. Wang, S.M. Bak, Y.S. Wu, Z.S. Wu, Y. Tian, X.Y. Xiong, Y. P. Li, W. Liu, S. Siahrostami, Y. Kuang, X.Q. Yang, H.H. Duan, Z.X. Feng, H. L. Wang, X.M. Sun, Introducing Fe2+ into nickel-iron layered double hydroxide: local structure modulated water oxidation activity, *Angew. Chem. Int. Ed.* 57 (2018) 9392–9396.
- [35] C. Tang, H.-S. Wang, H.-F. Wang, Q. Zhang, G.-L. Tian, J.-Q. Nie, F. Wei, Spatially confined hybridization of nanometer-sized NiFe hydroxides into nitrogen-doped graphene frameworks leading to superior oxygen evolution reactivity, *Adv. Mater.* 27 (2015) 4516–4522.
- [36] M.A. Oliver-Tolentino, J. Vázquez-Samperio, A. Manzo-Robledo, R.D. González-Huerta, J.L. Flores-Moreno, D. Ramírez-Rosales, A. Guzmán-Vargas, An approach to understanding the electrocatalytic activity enhancement by superexchange interaction toward OER in alkaline media of Ni-Fe LDH, *J. Phys. Chem. C* 118 (2014) 22432–22438.
- [37] M. Görlin, P. Chernev, J. Ferreira de Araújo, T. Reier, S. Dresp, B. Paul, R. Krähnert, H. Dau, P. Strasser, Oxygen evolution reaction dynamics, Faradaic charge efficiency, and the active metal redox states of Ni-Fe oxide water splitting electrocatalysts, *J. Am. Chem. Soc.* 138 (2016) 5603–5614.
- [38] J.-P. Jolivet, E. Tronc, C. Chanéac, Iron oxides: from molecular clusters to solid. A nice example of chemical versatility, *C. R. Geosci.* 338 (2006) 488–497.
- [39] S. Ye, Z. Shi, J. Feng, Y. Tong, G. Li, Activating CoOOH porous nanosheet arrays by partial iron substitution for efficient oxygen evolution reaction, *Angew. Chem. Int. Ed.* 57 (2018) 2672–2676.
- [40] W. Zheng, M. Liu, L.Y.S. Lee, Electrochemical instability of metal-organic frameworks: in situ spectroelectrochemical investigation of the real active sites, *ACS Catal.* 10 (2020) 81–92.



- [41] Y. Lei, T. Xu, S. Ye, L. Zheng, P. Liao, W. Xiong, J. Hu, Y. Wang, J. Wang, X. Ren, C. He, Q. Zhang, J. Liu, X. Sun, Engineering defect-rich Fe-doped NiO coupled Ni cluster nanotube arrays with excellent oxygen evolution activity, *Appl. Catal. B Environ.* 285 (2020), 119809.
- [42] S. Ye, J. Wang, J. Hu, Z. Chen, L. Zheng, Y. Fu, Y. Lei, X. Ren, C. He, Q. Zhang, J. Liu, Electrochemical construction of low-crystalline CoOOH nanosheets with short-range ordered grains to improve oxygen evolution activity, *ACS Catal.* 11 (2021) 6104–6112.
- [43] S.N. Sun, H.Y. Li, Z.C.J. Xu, Impact of surface area in evaluation of catalyst activity, *Joule* 2 (2018) 1024–1027.
- [44] Y. Duan, S.N. Sun, Y.M. Sun, S.B. Xi, X. Chi, Q.H. Zhang, X. Ren, J.X. Wang, S.J. H. Ong, Y.H. Du, L. Gu, A. Grimaud, Z.C.J. Xu, Mastering surface reconstruction of metastable spinel oxides for better water oxidation, *Adv. Mater.* 31 (2019), 1807898.
- [45] A. Grimaud, O. Diaz-Morales, B.H. Han, W.T. Hong, Y.L. Lee, L. Giordano, K. A. Stoerzinger, M.T.M. Koper, Y. Shao-Horn, Activating lattice oxygen redox reactions in metal oxides to catalyze oxygen evolution, *Nat. Chem.* 9 (2017) 457–465.
- [46] Z.F. Huang, J.J. Song, Y.H. Du, S.B. Xi, S. Dou, J.M.V. Nsanzimana, C. Wang, Z.C. J. Xu, X. Wang, Chemical and structural origin of lattice oxygen oxidation in Co-Zn oxyhydroxide oxygen evolution electrocatalysts, *Nat. Energy* 4 (2019) 329–338.
- [47] W.L. Li, F.S. Li, H. Yang, X.J. Wu, P.L. Zhang, Y. Shan, L.C. Sun, A bio-inspired coordination polymer as outstanding water oxidation catalyst via second coordination sphere engineering, *Nat. Commun.* 10 (2019) 5074.
- [48] L.I. Krishtalik, The mechanism of the proton transfer: an outline, *Bba Bioenergetics* 1458 (2000) 6–27.
- [49] C. Feng, M.B. Faheem, J. Fu, Y. Xiao, C. Li, Y. Li, Fe-based electrocatalysts for oxygen evolution reaction: progress and perspectives, *ACS Catal.* 10 (2020) 4019–4047.
- [50] A. Moysiadou, S. Lee, C.-S. Hsu, H.M. Chen, X. Hu, Mechanism of oxygen evolution catalyzed by cobalt oxyhydroxide: cobalt superoxide species as a key intermediate and dioxygen release as a rate-determining step, *J. Am. Chem. Soc.* 142 (2020) 11901–11914.